



CHORUS

This is the accepted manuscript made available via CHORUS. The article has been published as:

# Probe of Rydberg-Atom Transitions via an Amplitude-Modulated Optical Standing Wave with a Ponderomotive Interaction

K. R. Moore and G. Raithel

Phys. Rev. Lett. **115**, 163003 — Published 16 October 2015

DOI: [10.1103/PhysRevLett.115.163003](https://doi.org/10.1103/PhysRevLett.115.163003)

# Probe of Rydberg-atom transitions via an amplitude-modulated optical standing wave with ponderomotive interaction

K. R. Moore\* and G. Raithel

*Applied Physics Program and Department of Physics, University of Michigan, Ann Arbor, MI 48109*

(Dated: September 22, 2015)

In ponderomotive spectroscopy an amplitude-modulated optical standing wave is employed to probe Rydberg-atom transitions, utilizing a ponderomotive rather than a dipole-field interaction. Here, we engage nonlinearities in the modulation to drive dipole-forbidden transitions up to the fifth order. We reach transition frequencies approaching the sub-THz regime. We also demonstrate magic-wavelength conditions, which result in symmetric spectral lines with a Fourier-limited peak at the line center. Applicability to precision measurement is discussed.

Measurements of atomic transition frequencies are the cornerstone of precision metrology, used in applications ranging from atomic clocks [1] to measuring gravitational redshifts [2] and the radius of the proton [3]. An important metric of precision in these applications is the fractional frequency resolution,  $\Delta\nu/\nu$ , in which  $\nu$  is the measured frequency and  $\Delta\nu$  is its uncertainty. In order to obtain the best  $\Delta\nu/\nu$ , it is desirable to increase  $\nu$  while decreasing  $\Delta\nu$ . In recently-developed ponderomotive spectroscopy [4], Rydberg atoms are trapped in a standing-wave laser field (optical lattice). Electronic transitions are driven by modulating the lattice-light intensity at the transition frequencies of interest. In this Letter, we employ nonlinearities intrinsic to this excitation process to increase  $\nu$  by driving atomic transitions at higher harmonics of the modulation frequency. We also identify magic transitions that minimize trap-induced line shifts and reduce the uncertainty  $\Delta\nu$  by about one order of magnitude.

The ponderomotive interaction of a Rydberg electron with an optical field allows one to drive transitions when there is substantial spatial variation of the field intensity within the volume of the atom and when the lattice potential is modulated in time at a resonant transition frequency between states. The interaction Hamiltonian (in a.u.) is [5]

$$\hat{H} = \mathbf{A}(\hat{\mathbf{r}}) \cdot \hat{\mathbf{p}} + \mathbf{A}(\hat{\mathbf{r}}) \cdot \mathbf{A}(\hat{\mathbf{r}})/2, \quad (1)$$

where  $\hat{\mathbf{p}}$  is the electron's momentum operator and  $\mathbf{A}$  the vector potential of the laser field. In this work, the  $\mathbf{A} \cdot \mathbf{A}$  (ponderomotive) interaction drives atomic transitions, leading to flexible selection rules [6] and expanding the range of accessible transitions.

In Fig. 1 we show the experimental set-up. See [4] for details. A continuous-wave (c.w.) 1064-nm laser beam is split by a Mach-Zehnder interferometer into a low-power and higher-power beam. The low-power beam is amplitude-modulated via an EOM driven by a microwave signal with voltage amplitude  $V_\mu$  and frequency  $\Omega_1$ . This beam is coherently re-combined with the unmodulated (higher-power) beam to parametrically amplify the modulation sidebands [the radical term in Eq. (2)]. We form a

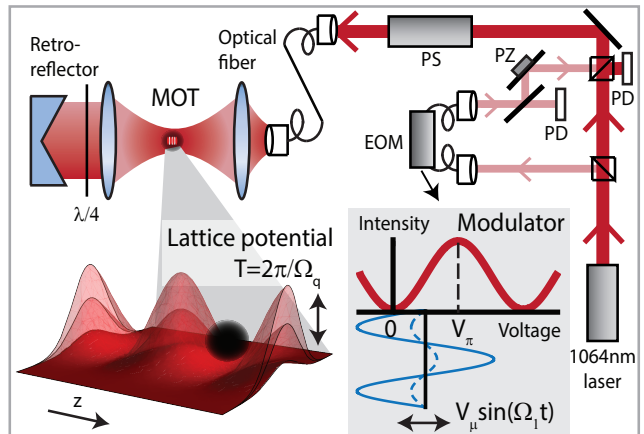


FIG. 1. Experimental set-up. A Mach-Zehnder interferometer splits and re-combines a 1064-nm c.w. beam. One portion is amplitude-modulated by a fiber-based electro-optic modulator (EOM), driven at frequency  $\Omega_1$  (inset). Locking is achieved via photodetectors (PD) and a piezo-electric transducer (PZ), described in [4]. Optional lattice inversion is achieved via a phase shifter (PS) and  $\lambda/4$  plate, described in [7]. The optical lattice is formed by retro-reflecting and focusing the beam into a  $^{85}\text{Rb}$  magneto-optical trap (MOT). The lattice modulation period in  $q$ th order is  $T = 2\pi/(q\Omega_1)$ .

standing-wave optical lattice in the atom-field interaction region by retro-reflecting the lattice beam. The ground-state atoms are collected and cooled at lattice intensity maxima. We laser-excite Rydberg atoms such that their center-of-mass locations are either at lattice intensity minima or maxima. This is accomplished by optional inversion of the optical lattice potential, effected by a phase shifter and a  $\lambda/4$  plate (see Fig. 1 and [7]). Intensity modulation of the lattice then results in a time-periodic atom-field ponderomotive interaction with a leading quadratic dependence on position.

Temporal harmonics in the lattice modulation drive transitions at frequencies  $\Omega_q = q\Omega_1$ , where  $q$  is an integer. The EOM offset voltage is set to  $V_\pi/2$  (see inset in Fig. 1). To modulate at the fundamental frequency  $\Omega_1$ , one has  $V_\mu \lesssim V_\pi/2$  (dashed blue line). To access higher harmonics,  $V_\mu$  is increased (solid blue line). The

resultant frequency upconversion is described by

$$\frac{I_{\text{inc}}}{I_{\text{dc}}} = 1 + 2 \left( \frac{\eta}{2} + \eta \sum_{q=1,3,5,\dots}^{\infty} J_q \left( \frac{\pi V_{\mu}}{V_{\pi}} \right) \sin(q\Omega_1 t) \right)^{1/2} + \eta \left( \frac{1}{2} + \sum_{q=1,3,5,\dots}^{\infty} J_q \left( \frac{\pi V_{\mu}}{V_{\pi}} \right) \sin(q\Omega_1 t) \right), \quad (2)$$

the incident intensity  $I_{\text{inc}}$  at the location of the atoms, scaled by  $I_{\text{dc}}$  (the intensity of the unmodulated high-power beam). Here,  $\eta$  is the power ratio between the modulated and unmodulated beams in the interferometer. A Fourier analysis of Eq. (2) with  $\eta = 0.0077$  (typical experimental value) leads to the Rabi frequency for the  $q$ th harmonic as a function of modulation strength  $V_{\mu}/V_{\pi}$  (Fig. 2). The Rabi frequency is scaled by  $I_{\text{dc}}$  (in units of  $\text{W}/\text{m}^2$ );  $\sqrt{\varepsilon}$ , where  $\varepsilon$  is the ratio of the return and incident lattice-beam intensities ( $\varepsilon = 0.09$  experimentally); and  $D_{n,l,m}^{n',l',m}$ . The unitless matrix elements for the spatial coupling,  $D_{n,l,m}^{n',l',m}$ , have been obtained in [6]. Here, the Rabi frequencies are near 100 kHz.

The Rabi frequencies exhibit a sinusoidal dependence on position in the optical lattice [4] and, for even-parity transitions (our case), are maximal for atoms at lattice intensity maxima and minima. Since the peak Rabi frequencies in Fig. 2 drop slowly as a function of  $q$ , unlike in typical nonlinear spectroscopy, we do not need to increase  $I_{\text{dc}}$  to realize higher-order transitions, thereby avoiding increased light shifts. We utilize Fig. 2 to determine the  $V_{\mu}$  needed to achieve a high Rabi frequency at the harmonic order of interest. Atom-field interaction times are  $\approx 10 \mu\text{s}$ . We target  $S \rightarrow S$  transitions because they are insensitive to the MOT magnetic field (which is always on). Under traditional electric-dipole selection rules, these transitions would not be allowed in first-order perturbation theory. However, because we employ ponderomotive spectroscopy, typical selection rules do not apply [6].

In Fig. 3 we demonstrate driving the ponderomotive transition  $52S_{1/2} \rightarrow 53S_{1/2}$  via the third harmonic ( $q = 3$ ) of the lattice modulation. For this transition,  $D_{52S}^{53S} =$

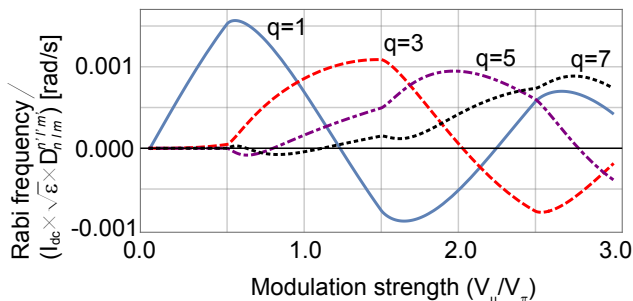


FIG. 2. Scaled Rabi frequencies of the  $q$ th harmonics of the lattice modulation at lattice intensity minima, as a function of  $V_{\mu}$  (units of  $V_{\pi}$ ) [8].

0.19, which is near the maximal value for  $nS \rightarrow (n+1)S$  transitions,  $D_{58S}^{59S} = 0.215$ . The inset in Fig. 3(a) shows that most spectral features can be reproduced by a semi-classical simulation. Details of the simulation can be found in [4] and [9]. The two outermost peaks are attributed to atoms that are anti-trapped (red-detuned peak) or trapped (blue-detuned peak) in the lattice [9]. The simulation does not reproduce the sharp central peak in the experimental spectrum.

To determine the line center, we fit the smoothed, averaged spectral line in Fig. 3(a) to a triple-Gaussian. To eliminate most of the trap-induced systematic shifts, we take the mean of the center locations of the outermost peaks. Assuming a perfect optical lattice, the outermost peaks correspond to equal but opposite extremum light shifts from the unperturbed Rydberg-Rydberg transition. Therefore, the mean provides a measurement of the transition line center with much-reduced light shift. See [9] for details. Results are summarized in Table I.

In Fig. 3(b) we show the dependence of the  $53S_{1/2}$  excited-state population on modulation strength  $V_{\mu}/V_{\pi}$ . The behavior qualitatively agrees with the square of the Rabi frequency for the  $q = 3$  curve in Fig. 2, plotted for comparison. In particular, significant excited-state populations only occur beyond a threshold value of  $V_{\mu}/V_{\pi} \approx 0.6$ . Fig. 3(b) reinforces that the spectrum in Fig. 3(a) is due to the nonlinear  $q = 3$  component of the lattice modulation.

To reach higher-frequency transitions, we drive transitions at higher  $q$ . In Fig. 4 we demonstrate the

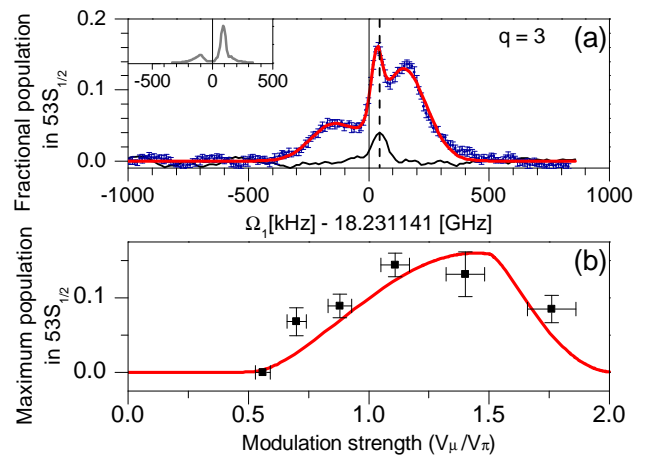


FIG. 3. Third harmonic drive. (a) Population in  $53S_{1/2}$  as a function of lattice modulation frequency  $\Omega_1$ . Data are a smoothed average of 10 scans with 200 measurements per frequency step. Error bars, s.e.m. Red curve, triple-Gaussian fit. Vertical black line, line center. Black dashed line, center location of a two-photon microwave spectroscopy measurement (black curve). Inset, simulation results. (b) Peak  $53S_{1/2}$  population as a function of modulation strength  $V_{\mu}$ . For each data point, 6-10 scans taken. Vertical (horizontal) error bars, peak height ( $V_{\pi}$ ) uncertainty. Red curve, proportional to the square of the  $q = 3$  curve in Fig. 2.

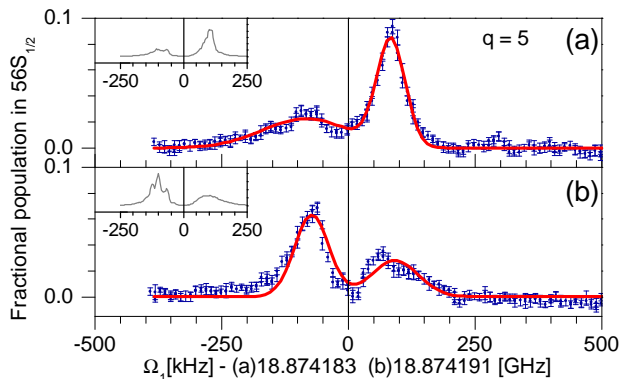


FIG. 4. Fifth harmonic drive. (a), (b) Population in  $56S_{1/2}$  as a function of lattice modulation frequency  $\Omega_1$  for Rydberg atoms prepared at lattice potential (a) minima (b) maxima. Data are a smoothed average of (a) 18 (b) 10 scans, 200 measurements each. Error bars, s.e.m. Red curve, double-Gaussian fit. Vertical black line, line center. Insets, simulation results.

ponderomotive transition  $54S_{1/2} \rightarrow 56S_{1/2}$ , which has  $D_{54S}^{56S} = 0.08$ , via the fifth harmonic ( $q = 5$ ). The spectra in Figs. 4(a), (b) are reproduced accurately by the simulations (insets). As before, the red-detuned (blue-detuned) peak is mostly due to atoms that are anti-trapped (trapped) in the lattice. We demonstrate the relation between Rydberg-atom position and light-shift polarity by preparing the Rydberg atoms either near a potential minimum [Fig. 4(a)], which results in mostly trapped atoms with positive light shifts; or maximum [Fig. 4(b)], which results in mostly anti-trapped atoms with negative light shifts [7].

To determine the line center, we fit the spectra in Figs. 4(a),(b) to a double-Gaussian. The mean of the center locations of the peaks yields a measurement in which the systematic light shifts mostly cancel. See Table I for results. The  $q = 5$  transition in Fig. 4 has a transition frequency of about 94.4 GHz. Hence, we are approaching the sub-THz regime, which is important for improving  $\Delta\nu/\nu$  in precision frequency measurements.

Magic-wavelength lattices play an important role because they allow for probing atoms in a light trap while avoiding systematic line-shifts due to the trap [10]. In a ponderomotive lattice, a magic condition occurs when a Rydberg atom becomes comparable in size to the lattice period. Then, the lattice-induced shifts of certain upper and lower Rydberg levels are nearly the same [11] and cancel. For Rb  $nS_{1/2}$  atoms in a 1064-nm lattice, this occurs for lower- and upper-level principal quantum numbers symmetric about 69.5. Furthermore, for principal quantum numbers between  $n = 66 - 73$  the sign of the effective polarizability of the atoms is reversed, indicating that Rydberg atoms are attracted to lattice-field maxima. This case differs from the more typical case where Rydberg atoms are attracted to field minima.

In Fig. 5 we drive the magic transition  $69S_{1/2} \rightarrow$

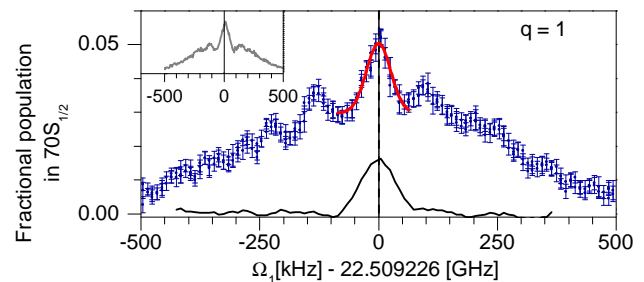


FIG. 5. Magic condition, fundamental. Population in  $70S_{1/2}$  as a function of lattice modulation frequency  $\Omega_1$ . Data are a smoothed average of 18 scans, 200 measurements each. Error bars, s.e.m. Red curve, single-Gaussian fit. Vertical black line, line center. Black dashed line, center location of a two-photon microwave spectroscopy measurement (black curve).

$70S_{1/2}$ , for which  $D_{69S}^{70S} = 0.13$ , at the fundamental frequency ( $q = 1$ ). The trap depths (light shifts) for both states are about the same (2.2% of the free-electron ponderomotive trap depth). The magic condition results in a lineshape that is symmetric and has a narrow central feature. These characteristics are well-reproduced by the simulation (inset). To determine the line center, we fit the central feature, expected to have nearly-zero systematic light shift, to a single Gaussian. This measurement has 2 kHz statistical uncertainty (see Table I).

In Fig. 6 we show a combination of both magic and nonlinear ponderomotive spectroscopy, which has the greatest potential to improve  $\Delta\nu/\nu$ . Here, we drive the magic transition  $68S_{1/2} \rightarrow 71S_{1/2}$ , which has  $D_{68S}^{71S} = 0.08$ , via the third harmonic ( $q = 3$ ). The trap depths for these states are both approximately 2.0% of the free-electron ponderomotive trap depth. The lineshapes are reproduced well by simulations (insets). In Fig. 6(a), we prepare the Rydberg atoms at trapping potential minima and observe a narrow central peak, the location of which agrees very well with the result of a two-photon microwave spectroscopy measurement (also shown). This peak is largely due to trapped atoms, which experience a Rabi frequency that is approximately fixed in amplitude and phase throughout the atom-field interaction time. This leads to a large pulse area and a central peak at zero detuning.

We attribute other features observed in Fig. 6 to the effect of atoms passing over the shallow lattice wells. The Rabi frequency then varies in time and flips sign at the lattice inflection points. In Fig. 6(b), we prepare the atoms at lattice potential maxima. From here, the atoms are likely to traverse several wells during the interaction time, resulting in several flips of the Rabi-frequency sign. This leads to a rotary-echo-like effect [12], i.e. small net pulse area and transition probability. A small non-zero detuning (partially) negates the echo effect. Hence, in Fig. 6(b) a central dip is observed.

The small oscillations near the central peak in Fig. 5 (and to a lesser extent in Fig. 6) are also due to un-

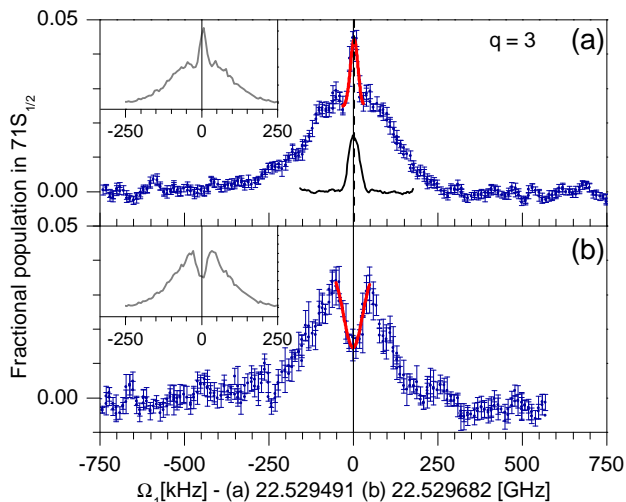


FIG. 6. Magic condition, third harmonic. Population in  $71S_{1/2}$  as a function of lattice modulation frequency  $\Omega_1$ . Data are a smoothed average of (a) 12 (b) 5 scans, 200 measurements each. Error bars, s.e.m. Red curve, single-Gaussian fit. Vertical black line, line center. (a) Lattice not inverted. Black dashed line, center location of a two-photon microwave spectroscopy measurement (black curve). (b) Lattice inverted.

trapped atoms traversing multiple wells. The interplay between consecutive Rabi-frequency sign-flips at the lattice inflection points and the detuning-induced phase  $\Delta\Omega_1 t$  causes the detuning-dependent oscillations.

Because both Figs. 5-6 correspond to a magic condition, we expect the respective frequency measurements, based on the central peaks, to have nearly-zero light shift. In both cases, the symmetry of the lineshapes agrees with our expectation. We attribute the  $\approx 200$  kHz discrepancy observed between Fig. 6(a) and (b) to differing residual electric fields, causing different systematic DC shifts between the data sets (which were taken on different days).

In both Figs. 5-6 the central peaks in the lattice-modulation spectra and the peaks in the two-photon reference spectra are at Fourier-limited resolution. Therefore, precision measurements made via magic-condition ponderomotive spectroscopy and traditional microwave spectroscopy can have similar spectral resolution. However, nonlinear ponderomotive spectroscopy allows us to access a wider variety of typically-forbidden transitions at high frequencies.

In Table I we summarize transition frequencies ( $q\Omega_1$ ) measured in the modulated lattice, expected transition frequencies ( $\nu_{\text{th}}$ ) calculated using quantum defects from [13], and reference measurements ( $2\nu_{2p}$ ) obtained via two-photon microwave spectroscopy in the absence of a lattice. The terms in brackets represent  $\Delta\nu/\nu$  for each frequency value. Overall, agreement is quite satisfactory. Statistically significant shifts in the measured results from the calculated values are negative, indicating possible Stark shifts due to residual DC electric fields. In the magic-condition cases, the statistical uncertainty in

	$q\Omega_1$ (GHz)	$\nu_{\text{th}}$ (GHz)	$2\nu_{2p}$ (GHz)
$52S_{1/2} \rightarrow 53S_{1/2}$ $q=3$	54.693423(15) [ $2.7 \times 10^{-7}$ ]	54.693577(5) [ $9 \times 10^{-8}$ ]	54.693556(6) [ $1 \times 10^{-7}$ ]
$54S_{1/2} \rightarrow 56S_{1/2}$ $q=5$	a. 94.370915(15) [ $1.6 \times 10^{-7}$ ]	94.371060(8) [ $8 \times 10^{-8}$ ]	
	b. 94.370955(15) [ $1.6 \times 10^{-7}$ ]	94.371060(8) [ $8 \times 10^{-8}$ ]	
$69S_{1/2} \rightarrow 70S_{1/2}$ $q=1$	22.509226(2) [ $9 \times 10^{-8}$ ]	22.509227(1) [ $4 \times 10^{-8}$ ]	22.509226(2) [ $9 \times 10^{-8}$ ]
$68S_{1/2} \rightarrow 71S_{1/2}$ $q=3$	a. 67.588473(2) [ $3 \times 10^{-8}$ ]	67.589048(4) [ $6 \times 10^{-8}$ ]	67.588478(1) [ $1 \times 10^{-8}$ ]
	b. 67.589046(9) [ $1 \times 10^{-7}$ ]	67.589048(4) [ $6 \times 10^{-8}$ ]	

TABLE I. Summary of results. All measurement uncertainties, statistical. Transitions below the double-line divider are magic. Quantities in brackets are  $\Delta\nu/\nu$ . See text for details.

$q\Omega_1$  is on the same order as the uncertainty in  $2\nu_{2p}$ .

Our data show that in magic-lattice spectroscopy on trapped atoms the statistical uncertainties are transform-limited. Therefore, nonlinear magic-condition ponderomotive spectroscopy improves the fractional frequency resolution  $\Delta\nu/\nu$  by increasing  $\nu$  by a factor of  $q$ . For a given atom-field interaction time  $T$  and transform-limited transitions,  $\Delta\nu/\nu$  improves from  $\approx 1/(T\Omega_1)$  to  $\approx 1/(qT\Omega_1)$ . With improved stray electric field control, the modulated lattice should be suitable for precision measurement of (dipole-forbidden) atomic transitions at high frequencies.

In conclusion, we have performed ponderomotive spectroscopy of Rydberg atoms by employing higher harmonics of the lattice modulation. The nonlinearity intrinsic to the lattice modulation has allowed us to reach transition frequencies  $\nu$  near the sub-THz regime, with the potential to exceed that limit, using modulation sources that are much lower in frequency. Using magic lattices, we have demonstrated Fourier-limited spectral lines with a small  $\Delta\nu$ , as well as reduced light shifts. Being able to access sub-THz atomic transitions with low  $\Delta\nu$  and free from light shifts will improve the fractional resolution ( $\Delta\nu/\nu$ ) of transition frequency measurements. Applications include precision measurement of atomic characteristics [14] and physical constants (e.g. the Rydberg constant [15], which could lead to verification of the proton size [3]).

This work was supported by NSF Grant No. PHY-1205559, NIST Grant No. 60NANB12D268, and NASA Grant No. NNN12AA01C. \*kaimoore@umich.edu

- 
- [1] B. Bloom, T. Nicholson, J. Williams, S. Campbell, M. Bishof, X. Zhang, W. Zhang, S. Bromley, and J. Ye, *Nature* **506**, 71 (2014).
- [2] C. W. Chou, D. B. Hume, T. Rosenband, and D. J. Wineland, *Science* **329**, 1630 (2010).
- [3] R. Pohl, A. Antognini, F. Nez, F. D. Amaro, F. Biraben, J. M. Cardoso, D. S. Covita, A. Dax, S. Dhawan, L. M. Fernandes, *et al.*, *Nature* **466**, 213 (2010).
- [4] K. R. Moore, S. E. Anderson, and G. Raithel, *Nat. Comm.* **6** (2015).
- [5] J. Sakurai, *Advanced Quantum Mechanics* (Addison-Wesley Publishing Company. Reading, Massachusetts, 1967) pp. 36–53.
- [6] B. Knuffman and G. Raithel, *Phys. Rev. A* **75**, 053401 (2007).
- [7] S. E. Anderson, K. C. Younge, and G. Raithel, *Phys. Rev. Lett.* **107**, 263001 (2011).
- [8] We do not plot even-order harmonics in Fig. 2 because in our set-up the modulated EOM voltage is centered at  $V_{\pi}/2$  (see Fig. 1), and therefore odd orders dominate the modulation spectrum.
- [9] See Supplemental Material [url], which includes Refs. [16]-[17].
- [10] J. Ye, H. J. Kimble, and H. Katori, *Science* **320**, 1734 (2008).
- [11] S. K. Dutta, J. R. Guest, D. Feldbaum, A. Walz-Flannigan, and G. Raithel, *Phys. Rev. Lett.* **85**, 5551 (2000).
- [12] K. C. Younge and G. Raithel, *New Journal of Physics* **11**, 043006 (2009).
- [13] M. Mack, F. Karlewski, H. Hattermann, S. Höckh, F. Jessen, D. Cano, and J. Fortágh, *Phys. Rev. A* **83**, 052515 (2011).
- [14] J. Han, Y. Jamil, D. V. L. Norum, P. J. Tanner, and T. F. Gallagher, *Phys. Rev. A* **74**, 054502 (2006).
- [15] R. Lutwak, J. Holley, P. P. Chang, S. Paine, D. Kleppner, and T. Ducas, *Phys. Rev. A* **56**, 1443 (1997).
- [16] K. Younge, S. E. Anderson, and G. Raithel, *New J. Phys.* **12** (2010).
- [17] S. E. Anderson and G. Raithel, *Phys. Rev. Lett.* **109**, 023001 (2012).